Design and Analysis of MEMS based Accelerometer for Automatic Detection of Railway Wheel Flat

Rajib Ul Alam Uzzal, Ion Stiharu , Waiz Ahmed

Abstract—This paper presents the modeling of a MEMS based accelerometer in order to detect the presence of a wheel flat in the railway vehicle. A haversine wheel flat is assigned to one wheel of a 5 DOF pitch plane vehicle model, which is coupled to a 3 layer track model. Based on the simulated acceleration response obtained from the vehicle-track model, an accelerometer is designed that meets all the requirements to detect the presence of a wheel flat. The proposed accelerometer can survive in a dynamic shocking environment with acceleration up to $\pm150g$. The parameters of the accelerometer are calculated in order to achieve the required specifications using lumped element approximation and the results are used for initial design layout. A finite element analysis code (COMSOL) is used to perform simulations of the accelerometer under various operating conditions and to determine the optimum configuration. The simulated results are found within about 2% of the calculated values, which indicates the validity of lumped element approach. The stability of the accelerometer is also determined in the desired range of operation including the condition under shock.

Keywords—MEMS accelerometer, Pitch plane vehicle, wheel flat.

I. INTRODUCTION

WHEEL flat is the most common type of wheel defect encountered by railway industry, which develops due to sliding of the wheel on the rail under braking, when the braking force is larger than the available wheel/rail friction or when the brake system poorly adjusted or defective [1]. During sliding, part of the wheel tread could be removed causing a flat surface to form on the wheel profile. This surface irregularity causes impact loads on the rail and track structure as the wheel rolls. This impact load induces high frequency vibration of the track and the vehicle components. It has been suggested that excessive magnitude of the impact load may even shear the rail [2].

Rajib Ul Alam Uzzal is a Graduate Research Student (Ph.D) in Mechanical Engineering Department, Concordia University, Montreal, Canada, phone: 1-514-848-2424 Ex. 7942; fax: 1-514- 848-3175; e-mail: rajiboic@gmail.com.
Ion Stiharu is a Professor in Mechanical Engineering Department, Concordia University, Montreal, Canada, e-mail: istih@alcor.concordia.ca.
Waiz Ahmed is a Professor in Mechanical Engineering Department, Concordia University, Montreal, Canada, e-mail: waiz@alcor.concordia.ca

A number of studies have attributed the wheel sliding to poorly adjusted, frozen, or locked wheels or excessive braking forces in relation to the wheel/rail adhesion [3]. Contaminations on the rail surface, such as leaves, grease, frost, and snow could also aggravate the sliding at the wheel-rail contact. Jergeus et al. reported in [3] that the area of actual wheel/rail contact changes during the formation of a flat and thus the shape of the railhead also have great influence on the growth of the wheel flat.

With continuing increases in the axle loads and operating speed, the wheel flats are becoming increasingly common. The high magnitude of impacts due to wheel flats, whether single or multiple, not only induce high magnitude impact force and stress on vehicle components but also to the rails and the sleepers [4]. Wheel flats thus affect track maintenance and the reliability of the vehicle's rolling elements. In addition to safety and economic considerations, these defects affect passenger comfort and significantly increase the intensity of noise. A damaged bearing that seizes can also cause skidding. The high impact forces from a flat wheel cause stress in the rail, and in extreme cases can break the track or cause the wheel to jump off the track, resulting in a derailment. The contact forces are quite high; therefore, damage and wear are consistently relevant, mainly due to the great weights involved in the rail traffic and to the hardness of rail and wheel materials. It is clear that the continuous repetitions of impacts on rail, together with the high forces involved, cause rapid deterioration of, both, rolling and fixed railway equipments. If ignored or underestimated, the fault will wear out materials up to the breakdown. Various methods have been proposed for detecting flat wheels. One method is to employ inspectors to listen to the trains as they move through a particular location. Some flat wheels are found through routine inspections when the cars are being serviced. A wide range of sensors has been proposed for detecting flat wheels. These employ a range of technologies from optical systems that gauge the wheels in real time to sensors that look for vibrations and stress.

Belotti et al. [5] has shown a wheel-flat diagnostic tool by using wavelet transform method. In this study, an experimental layout is designed in order to provide the information, to develop and to validate a reliable, effective, and low-cost wheel-flat diagnostic tool. The method implies the detection of the wheel flats through the measurement of peak acceleration using several accelerometers placed in the fixed position of the rail. The result obtained from experimental study validates the theoretical model and

World Academy of Science, Engineering and Technology
International Journal of Mechanical and Mechatronics Engineering
Vol:3, No:5, 2009

demonstrates the advantages of wavelet-based signatures detection. However, the wired connections between the accelerometer and the analysis house make the overall system rather unreliable. Furthermore, the entire train has to pass through the specific test section that can be far from the train operating area. The detection of wheel flats with fiber optic sensors has been reported by Anderson [6]. In this method, the screen is fixed between the end of the fiber and the active area of the detector, and the pinhole is sized to have the same diameter as the RMS value of the bright/dark spots in the speckle pattern. When the fiber is disturbed the speckle pattern changes and as the speckle pattern changes, bright and dark fringes pass over the pinhole, resulting in a time varying signal that is indicative of the vibration of the fiber. For small perturbations, the frequency of this signal is equal to the frequency of the physical disturbance. The advantage of the pinhole/detector system is low cost and simplicity. However, the design has poor optical efficiency, wasting up to 90% or more of the incident light, which is attributed to the limiting aperture of the pinhole. Furthermore, the placement of the fiber on the underside of the metal grating alongside the track makes the system rather complicated.

Another method of detecting wheel flats employs scanning with laser beam [7]. The entire module consists of a detector to send and receive radiation signals after the scanning of the wheel; a smart electronics box (SEB) that contains digital signal processors and connection to the wayside PC for further analysis. Wheel flats can be clearly detected from the unique signature and the gradients between scans at different heights on the wheel. An acoustic method for detection of wheel flats is also presented in literature [8]. In this method, sound from a passing train is recorded and the particular sound caused by the impact between a wheel flat and the supporting rail is distinguished by detecting frequencies in that particular sound. Another method for detection of the presence of the wheel flats relies on the sensing of changes in voltage resulting from a break in the established circuit caused by the wheel flat.

From the review of the relevant literature, it is evident that considerable efforts have been made to detect the presence of flats in the wheel. However, all these detection techniques utilize an instrumented railway track equipped with the sensors, which requires the train to pass through that particular section of the rail in order to investigate the wheel flat. The above presented methods are unsuitable for a train in operation that needs prompt investigation. Furthermore, the present techniques require large connections of wires to transfer the data from the test section to analysis center. One of the challenges for sensors is the need to operate remotely in harsh environments with exposure to wide temperature ranges as well as rain, snow, slush, dirt and grime. These findings form the basis of the present study to design an accelerometer that will be placed on the wheel bearing and able to detect continuously the wheel defect. In the present paper, a 5-DOF rail vehicle coupled with a 3-layer track model is developed in order to investigate the acceleration level at the wheel-rail contact point in the presence of a wheel flat. This vehicle model will consider the pitch effect, which is significant in the presence of a flat. An idealized haversine wheel flat with the rounded corner is included in the wheel-rail contact model. A

MATALB predefined code "ode45" has been employed to perform the time domain analyses of dynamic responses of the coupled system. A MEMS based sensor is modeled that can detect the peak acceleration due the wheel-rail impact. A commercially available software COMSOL is employed in order to validate the developed accelerometer model. The simulated responses are compared with the results obtained from the calculation. Finally, the stability and maximum stress level of the accelerometer are estimated in order to ensure the safe operation of the sensor.

II. MATHEMATICAL MODELING

A. Vehicle and track model

This study is primarily concerned with the vertical wheel-rail impact load associated with vertical dynamics of the coupled railway vehicle and track structure system. In general, a vehicle-track system model for simulation of vertical dynamic interactions is composed of a vehicle model, track model and the contact model with rail and wheel irregularities. It has been suggested that the vertical dynamics of the vehicle alone contributes only little to the wheel-rail impact force [9]. The vehicle model may thus be greatly simplified to ensure representative wheel loads and their variations. In this study, the vehicle system is modeled as a 5-DOF lumped mass model comprising a quarter of the car body and half of the bogie coupled to two wheels through the primary suspension. The analysis of dynamic impact loads, however, necessitates a most comprehensive modeling of the continuous track system [9]. In this study, a multiple-layer track system model comprising the rail pads, the ballasts, and the subgrade is considered to study the coupled rail-vehicle system dynamics in the presence of wheel defects.

The dynamic model used in this study to investigate the vehicle-track response in vertical direction thus consists of a 5 DOF vehicle model coupled with a 3-layer track system. The coupling between the vehicle and track is achieved by the non-linear Hertzian contact model. The complete vehicle-track interaction model is shown in Fig. 1. The primary and secondary suspension connecting the wheels and bogie frame, and the bogie frame and the car body respectively are modeled as spring and damper elements. In this study, a 3-layer 2D track system model consisting of single rail of 100 sleepers/ballasts length is employed, based on the assumption that the track is symmetric with respect to its centerline. The rail is discretely supported by sleepers, ballasts/subballasts and subgrades. The two layers of discrete masses below the rail represent the sleeper and the ballast respectively. The rail beam is modeled as an Euler-Bernoulli beam, which has been shown [10] to be effective for practical operational frequency range.

As shown in Fig. 1, the rail beam is supported on the discrete spring damper system representing for rail pads and fasteners. Railpads are placed between the steel rails and the sleepers to protect the sleepers from wear and impact damage, and further provide electrical insulation of the rails. The rail is connected to the rigid sleeper's masses, which provide support

World Academy of Science, Engineering and Technology
International Journal of Mechanical and Mechatronics Engineering
Vol:3, No:5, 2009

for the rails and preserve level, and alignment of the track through the rail pad to protect the sleeper from impact damage. The ballast is modeled as combination of the mass, spring and damper system. The ballast blocks are interconnected elastically, so that a vertical deflection of one ballast block will spread to others via shear springs and dampers.

In order to simulate the wheel-rail interaction force, the contact between the wheel and rail must be established by a well-defined method, since an accurate solution of the rolling contact problem is quite complex. The interaction between the vehicle and the track system is achieved at the wheel/rail interfaces through wheel/rail force compatibility. The wheel-rail contact has been widely described by the nonlinear Hertzian contact theory commonly used in the wheel/rail interaction problems [4]. Yan and Fischer [11] have analyzed applicability of the Hertz contact theory to wheel-rail contact problems and concluded that the wheel-rail contact dynamics can be described with reasonable accuracy for purely elastic contact when the surface curvature of the rail within the contact area remains unchanged.
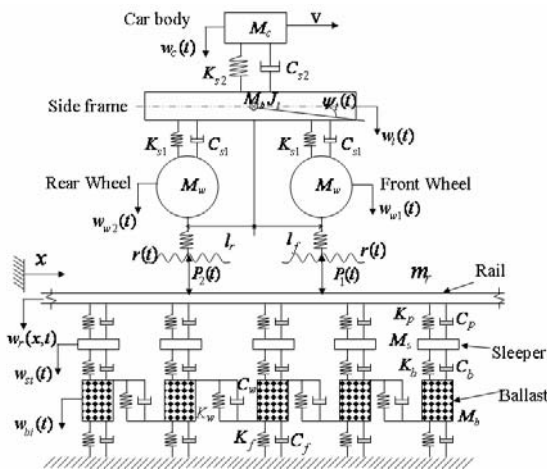

Fig.1 Vehicle and track system model

The detailed descriptions of the mathematical model combined with the equations of motion for the vehicle and track system can be obtained in reference [12]. The final forms of the equations for vehicle and track subsystem are as follows:

Vehicle subsystem: $M_V \ddot{d}_V + C_V \dot{d}_V + K_V d_V = F_{VT}$ (1)

Track subsystem: $M_T \ddot{d}_T + C_T \dot{d}_T + K_T d_T = F_{VT}$ (2)

Wheel-rail interface subsystem: $F_{VT} = C_H (\Delta Z)^{3/2}$ (3)

Where M_V, C_V and K_V are mass, damping and stiffness matrices of the vehicle subsystem respectively. d_V, $\dot{d}_V$, $\ddot{d}_V$ are displacement, velocity and acceleration vectors of the vehicle subsystem respectively. F_{VT} is the interface force vector between the vehicle and track subsystem. M_T, C_T and K_T are mass, damping and stiffness matrices of the track

subsystem respectively. d_T, $\dot{d}_T$ and $\ddot{d}_T$ are displacement, velocity and acceleration vectors of the track subsystem respectively. ΔZ is the wheel-rail overlap in the vertical direction and C_H is the Hertzian constant.

B. Wheel flat model

A wide range of mathematical descriptions has been evolved to characterize the geometry of wheel flats in order to investigate the impact loads [[2], [4], [9]]. The wheel flats have been classified as chord type flat, cosine type flat and combined flat. On the basis of the reported flat geometries, the wheel flat can be divided into two categories: (i) chord type flat; and (ii) haversine type flat. The former one represents a freshly formed flat, while the latter is used to describe the geometry of the flat on the wheel in service that yields rounded edges [12].

After formation of a wheel flat, the sharp edges at the end of the profile of a fresh profile become rounded, while continued in service. This type of flat is commonly known as haversine flat, which is shown in Fig. 2.
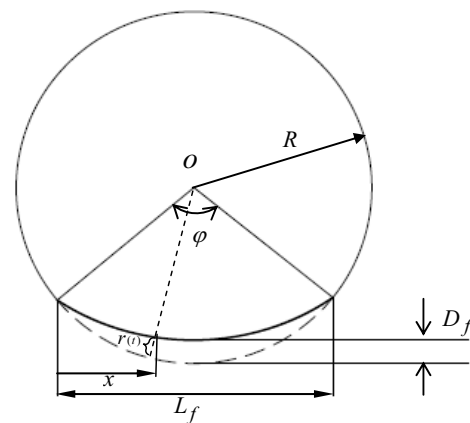

Fig. 2 A haversine type wheel flat [12]

The variation in the radii of a contact point $r(t)$ within a haversine flat is expressed as:

$$r(t) = \frac{1}{2} D_f [1 - \cos(2\pi x / L_f)] \qquad (4)$$

Where D_f is the flat depth that has been related to wheel radius R, in the following manner [9]:

$$D_f = L_f^2 /(16R) \qquad (5)$$

Equations (1-3) coupled with Equation (4) are simultaneously solved together in order to obtained the acceleration level of the wheel in the presence of a flat.

III. DYNAMIC ANALYSIS OF WHEEL IN THE PRESENCE OF A FLAT

In order to design of an accelerometer, the peak acceleration of the wheel and the frequency bandwidth in the presence of a flat is required to be known for selection of the operating range of the accelerometer. Thus, the coupled vehicle-track system developed at the previous section is

World Academy of Science, Engineering and Technology
International Journal of Mechanical and Mechatronics Engineering
Vol:3, No:5, 2009

simulated for a set of given parameters. In the simulation of the wheel-rail interaction, the contact is modeled with the consideration of the wheel lift-off from the rail. The nominal vehicle, track and flat parameters used for the simulations are presented in Table 1.

TABLE 1
NOMINAL SIMULATION PARAMETERS [4]

Symbol	Parameter	Value
M_c	Car body mass (quarter car)	19400 kg
M_t	Bogie mass (half)	500 kg
M_w	Wheel mass	500 kg
J_t	Bogie mass moment inertia	176 kg-m^2
K_{s1}	Primary suspension stiffness	788 MN/m
C_{s1}	Primary suspension damping	3.5 kN-s/m
K_{s2}	Secondary suspension stiffness	6.11 MN/m
C_{s2}	Secondary suspension damping	158 kN-s/m
l_t	Wheelset distance	1.25 m
R	Wheel radius	0.42 m
L_f	Flat length	52 mm
D_f	Flat depth	0.4 mm
C_H	Hertzian spring constant	87 GN/m$^{3/2}$
m_r	Rail mass per unit length	60.64 kg/m
EI	Rail bending stiffness	6.62 MN-m^2
M_s	Sleeper mass	118.5 kg
M_b	Ballast mass	739 kg
K_p	Railpad stiffness	120 MN/m
K_b	Ballast stiffness	182 MN/m
K_w	Ballast shear stiffness	147 MN/m
K_f	Subgrade stiffness	78.4 MN/m
C_p	Railpad damping	75 kN-s/m
C_b	Ballast damping	58.8 kN-s/m
C_w	Ballast shear damping	80 kN-s/m
C_f	Subgrade damping	31.15 kN-s/m
l_S	Sleeper distance	0.6 m
N	No. of sleepers	100

The time histories of the acceleration of the front wheel of the vehicle obtained from the simulation are shown in Fig. 3 for three different vehicle forward speeds (v = 30, 70 and 110 km/h), which covers the speed range of a freight car in Canada. A wheel flat of 52 mm length and 0.4 mm depth is considered that meets the wheel replacement criteria set by Association of American Railway (AAR) [13]. The static load acting on the wheel is 102 kN, which is the nominal load for a freight car system in North America. The figure shows that the peak acceleration of the wheel can be reached as high as 473.5 m/s^2 with a frequency bandwidth of around 500 Hz in the presence of a single haversine wheel flat for the selected speed range. After the first peak, the time history of acceleration shows several peaks which die out after about 0.0017s at a vehicle speed of 110 km/h. Thus, an accelerometer capable of

receiving this peak acceleration within the fraction of a second should be designed.
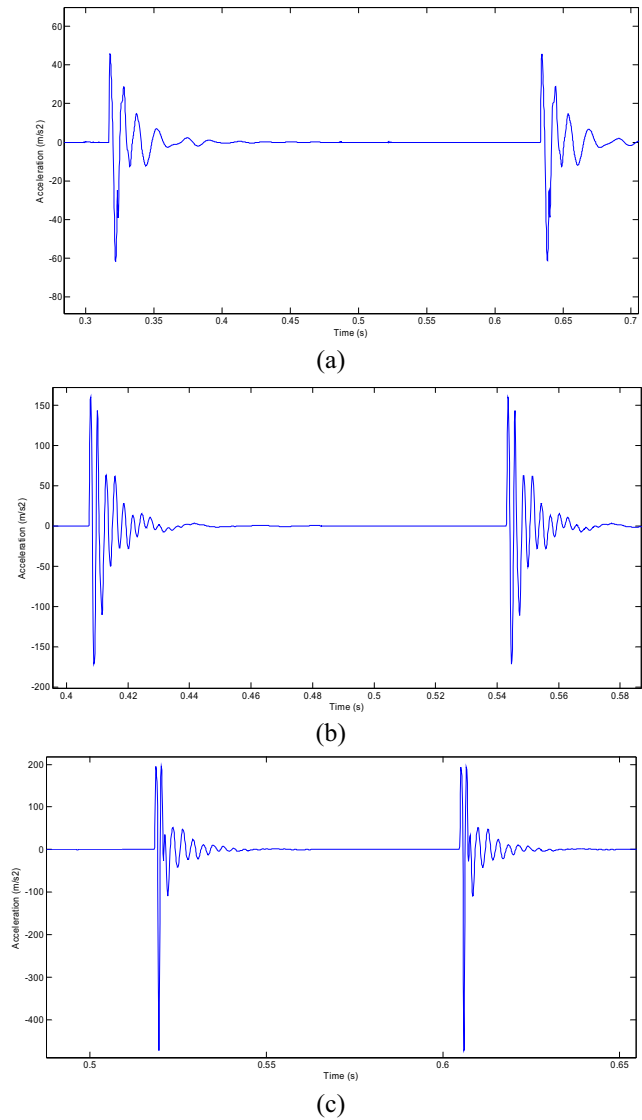

(a)

(b)

(c)

Fig. 3 Acceleration time history of a wheel in the presence of a rounded flat (L_f = 52 mm; D_f = 0.4 mm) at a speed of (a) 30 km/h; (b) 70 km/h and (c) 110 km/h.

IV. DESIGN OF THE ACCELEROMETER

It is apparent from the above section that the proposed accelerometer needs to sense the acceleration in the range of ±50 g in vertical direction while able to maintain a 10 kHz (20 times higher than the required bandwidth) frequency response. The accelerometer should be also able to survive a maximum shock of ±150 g in case of extreme condition. The design's layout should fit within an area of 1 cm2. The accelerometer should also survive in extreme temperature condition. In order to achieve the desired output, accurate design of each elements of the accelerometer is required. In this chapter, the analyses of the design of the various components are presented in order to satisfy the design requirements.

World Academy of Science, Engineering and Technology
International Journal of Mechanical and Mechatronics Engineering
Vol:3, No:5, 2009

A Spring

In an accelerometer, the displacement of the proof mass is restricted by the spring force. The displacement of the proof mass will compress one spring and stretch the other until the spring forces cancel the inertial force due to the acceleration. Thus, the combined spring constant of the springs will determine the amount of proof mass displacement and hence the signal generated by the sensing capacitors. Therefore, a suitable spring parameter is required to choose for accurate prediction of the accelerometer output. In MEMS, the most convenient way to make a spring is to use a folded structure as shown in Fig. 4 [14].
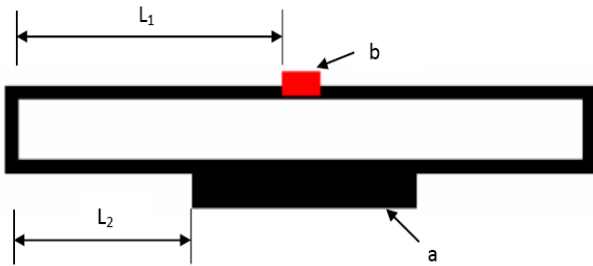
Fig. 4 Schematic diagram of a folded spring made of polysilicon [14].

The spring is composed of four beams made of polysilicon layers. The "b" marked area in Fig. 4 is the anchor, which fixes the spring on to the substrate. The central plate (proof mass) is connected from the "a" marked area to the other symmetrical spring. The spring constant (K) determined the extent of displacement of the proof mass and could be calculated by the formula in Equation (6) as given in [14].

$$K = (\frac{\pi^4}{6})[\frac{EWH^3}{(2L_1)^3 + (2L_2)^3}] \qquad (6)$$

Where E is the Young's modulus of polysilicon, W is the beam width, H is the beam thickness and L_1, L_2 are the beam lengths as shown in Fig. 4. From the above formula, it can be seen that the spring constant is strongly dependent on the lengths (L_1 and L_2) if H and W are fixed. Another important parameter in the design of an accelerometer is the proof mass (m) since the spring constant and proof mass determine the resonant frequency (ω_0) as given in Equation (7):

$$\omega_0 = 2\pi f = \sqrt{\frac{K}{m}} \text{ or, } m = \frac{K}{\omega_0^2} \qquad (7)$$

The resonant frequency determined how fast the accelerometer can respond to a change in acceleration or the bandwidth of operation. This study required the bandwidth to be 500 Hz and it is necessary to set the resonant frequency to be higher than the bandwidth to avoid unstable operation [15]. In the present design, the resonant frequency is set to be 20 times the bandwidth or 10 kHz. For simplicity, lengths L_1 and L_2 are assumed to be the same and the dimensions of W and H are also taken to be the same as the polysilicon layer thickness (2 μm). In order to estimate the proof mass that gives the resonant frequency of about 10 kHz, the total spring constant due to the two springs (2K) using Equation (6) is first

calculated. Thereafter, using the resonant frequency and the calculated spring constants, the mass of the proof mass is determined for different sets of L_1 and L_2. Several numbers of iterations are carried out in order to find out the mass of the proof mass. The analysis showed that in order to achieve 10 kHz resonant frequency, it is necessary to have $L_1 = L_2 = 150$ μm and proof mass of 2.924×10^{-10} kg. The total stiffness of the accelerometer (2K) is obtained as 1.1545 N/m.

B Proof mass and electrodes

The proof mass included the masses of the central plate and all the moving electrodes as illustrated in Fig. 5. In order to perform the self-test function, the whole structure is separated into two parts, the sensing region, and the self-test region.
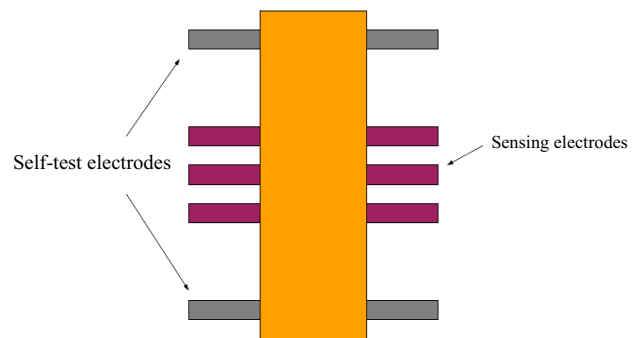

Fig. 5 Schematic diagram of proof mass with sensing and self-test electrodes.

Sensing region is responsible for detecting motion when the acceleration is applied. According to the previous calculation, the proof mass including the central plate and all of the connected electrodes should be limited to about 2.924×10^{-10} kg. The attached finger-like polysilicon structure in the central plate is the sensing element. The moving and fixed fingers formed a parallel plate capacitor and the capacitance can be estimated using Equation (8).

$$C = \frac{\varepsilon_r \varepsilon_0 A}{g_{ap}} \qquad (8)$$

Where ε_0 is the absolute permittivity, A is the total overlap area between all the fingers in the sensing region, and g_{ap} is the separation between adjacent fingers. Since the change in capacitance is proportional to the area (A), in order to achieve higher signal it is necessary to increase the area or number of fingers. By setting the value of the capacitance to be about 100 fF, the number of fingers required is about 80. The parameters used in this estimation are summarized in Table 2. These electrodes can be placed on either side of the proof mass as illustrated in Fig. 5.

In the self-test region, the design considerations are the same as that in the sensing region except for the applied voltages and number of electrodes. Approximately, 30% of the sensing electrodes (24) are selected for generating an internal electrostatic force for self-testing. These are located on both sides of the central plate and separated into 4 regions.

World Academy of Science, Engineering and Technology
International Journal of Mechanical and Mechatronics Engineering
Vol:3, No:5, 2009

Each region is made of 6 electrodes and the dimensions are same as those obtained in Table 2.

TABLE II
PARAMETERS OF MOVING ELECTRODES

Parameters	Electrodes design data
Total length	176 μm
Overlap length	141 μm
Width	2 μm
Depth	2 μm
Gap between fingers	2 μm
Permittivity	8.854×10^{-12} F/m
Density of the polysilicon	2330 kg/m^3

To achieve the required total mass, the dimensions of the central plate is determined by subtracting the mass of all the fingers (including the ones used for testing) and found to be 624 μm for length and 42.11 μm for width. The calculations of mass of the central plate and 104 electrodes are shown below.

$$m_{central} = \rho V = 624 \mu m \times 42.11 \mu m \times 2 \mu m \times 2330 kg/m^3$$

$$= 1.2167 \times 10^{-10} kg$$

$$m_{fingers} = 104 \times 2 \mu m \times 176 \mu m \times 2 \mu m \times 2330 kg/m^3$$

$$= 1.7077 \times 10^{-10} kg$$

$$m = m_{central} + m_{fingers} = 2.9243 \times 10^{-10} kg$$

Force on the proof mass is achieved by applying a DC voltage to the self-test capacitor. The amount of force as a function of supplied voltage (V_s) can be estimated using the stored energy (W) on the capacitor as followed:

$$W = \frac{1}{2} C V_s^2 \qquad (9)$$

Using Equation (9) the electrostatic force F can be found as

$$F = \frac{\partial W}{\partial g_{ap}} = \frac{\varepsilon_0 A V_s^2}{2 g_{ap}^2} \qquad (10)$$

If one plate is free and the other one is fixed in the parallel capacitor, it would mean that the free plate could be driven by electrostatic force. The force controlled by voltage is inversely proportional to g_{ap} and directly proportional to V_s^2. The force between each air of movable and fixed electrodes is given by Equation (10).

Combining Hook's law and Newton's second law as well as the effective spring constant, one could compute the displacement of the proof mass under the conditions of self-test, and under 50g and 150g of acceleration.

$$F = kx = ma \qquad (11)$$

Where k is the total stiffness of the accelerometer. Using the total mass of the proof mass of 2.924×10^{-10} kg, the deflections under 50g and 150g are found to be 1.242×10^{-7} m and 3.73×10^{-7} m, respectively. The corresponding voltages required for achieving above displacements using the self-test capacitor can be estimated using Equation (10) and found to be about 4.37 V and 7.58 V, respectively.

At this point, the preliminary design and operating parameters are set. These design parameters of the accelerometer were used to layout the design using COMSOL software as shown in Fig. 6. In addition to layout, COMSOL software was also used for finite element modeling of the designed software. COMSOL was then used to run simulations that took into account all the nonlinearities of the design and the results were used to perform analysis of the designed accelerometer. The 3-D views of the various components of the accelerometer are shown below in Fig. 7 to Fig. 9.
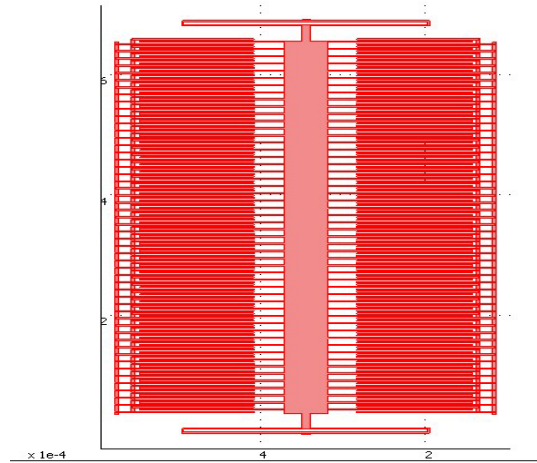

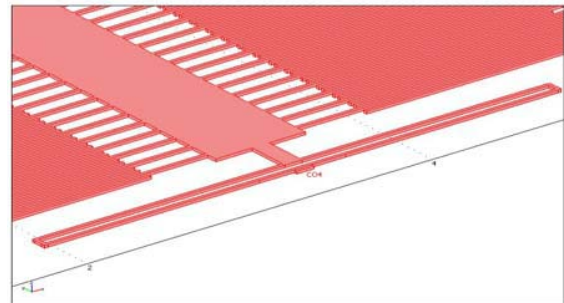Fig. 6 Schematic view of the proposed accelerometer

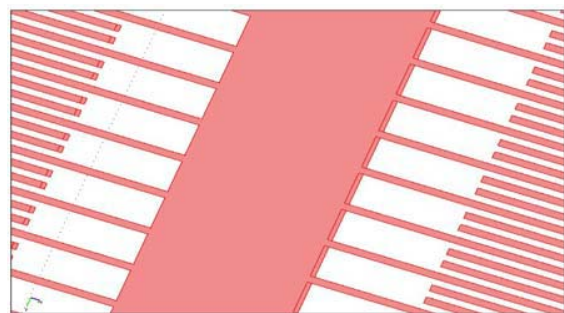Fig. 7 3-D highlighted view of the folded spring of the accelerometer in COMSOL

Fig. 8 3-D highlighted view of the moveable electrodes attached to the center plate in COMSOL
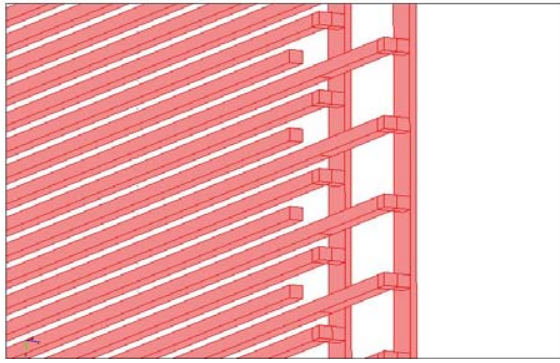
World Academy of Science, Engineering and Technology
International Journal of Mechanical and Mechatronics Engineering
Vol:3, No:5, 2009

Fig. 9 3-D highlighted view of the fixed electrodes of the
accelerometer in COMSOL

V. SIMULATIONS AND RESULTS

In order to perform a realistic simulation of the performance
of the accelerometer, the boundary conditions of the 3-D
model with the points of acting load are set up in COMSOL,
where the COMSOL would perform the simulation depending
on the various forces applied by the user. Since the proof mass
activates the movement due to acceleration, the supplied force
was also put on the central plate body and denoted as a force
point in COMSOL. The simulated results would show
displacements and stresses in vertical axis. According to the
requirements described in Section IV, the device should
survive 150g of acceleration – note that measurements at this
high acceleration level are not required, but it should survive
such shocks. The easiest way to make sure that it works is to
check whether the structure exceeds its stress limits under
150g of acceleration.

A. 50g Acceleration

The designed accelerometer is first analyzed under the
acceleration of 50g of acceleration applied on the proof mass.
The simulations were carried out in COMSOL. The simulated
results are shown in Fig. 10. In Fig. 10, the amount of
deflection is color corded with maroon being the highest
deflection. The maximum deflection is about 1.26×10^{-7} m.
The highlighted view of the local area of the springs shows
that the deflection is minimum near the anchors and increased
gradually towards the center of the spring where the proof
mass is connected. This response is similar to the preliminary
calculated result as presented in the previous chapter. The
difference between the preliminary calculations and the
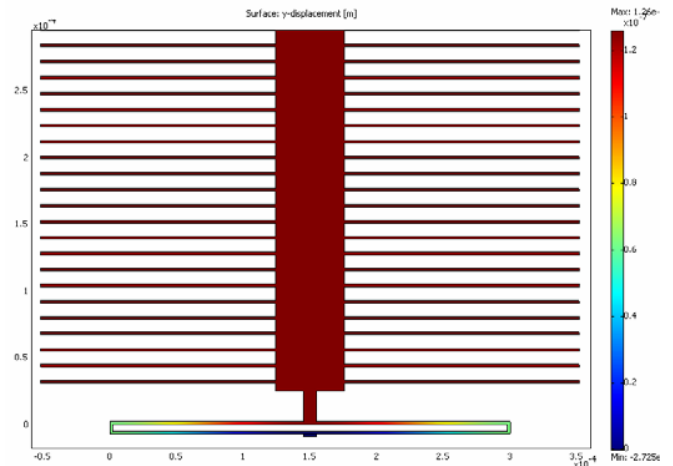COMSOL simulations is about 1.5%.

Fig. 10 Expanded view of the spring deflection under 50g
acceleration

B. 150g Acceleration

Similar to the 50g simulation, one could assume the
acceleration of 150g on the central plate. In this simulation, it
is necessary to pay attention to stresses in the beams of the
springs in addition to the displacements. Because the
connecting region of springs to the proof mass displayed the
maximum displacement, the COMSOL simulations were
carried out highlighting these sections as shown in Fig. 11.
The simulated results yielded displacement of about 3.76×10^{-7}
m along the direction of the force (y direction). This is about 3
times larger than the displacement under 50g force. The
calculated value is lower than the simulation by almost 1%.
The maximum stress in the anchor is found as 9.87 MPa as
shown in Fig. 12. This stress level is, however, far smaller
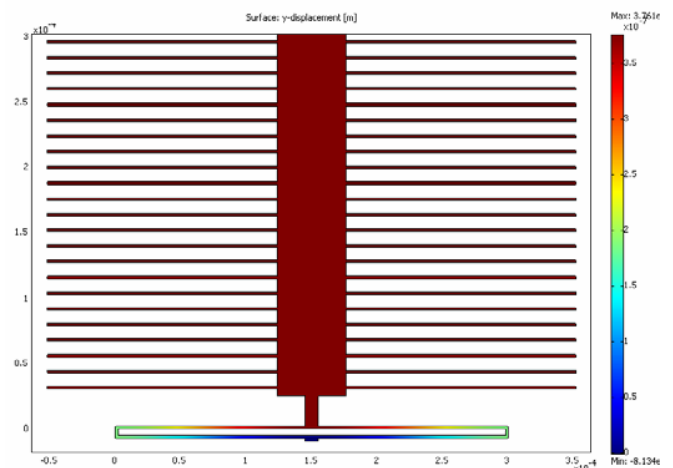than the material elastic limit of 130 MPa.

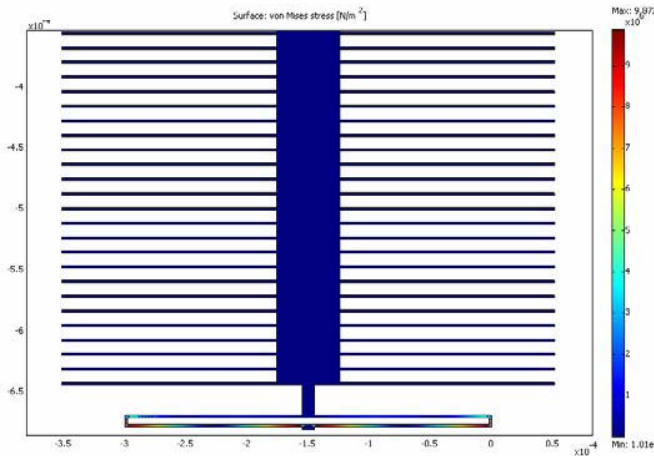Fig. 11 Expanded view of the spring deflection under 150g
acceleration

World Academy of Science, Engineering and Technology
International Journal of Mechanical and Mechatronics Engineering
Vol:3, No:5, 2009

Fig. 12 Stress in vertical direction under 150 g acceleration

VI. FUNCTIONAL ANALYSIS

A. Output voltage and displacement

The basic working principle of the accelerometer is based on the fact that under an external acceleration a proof mass is displaced a small distance, which changed the gap between the electrodes that behave as varying capacitors. The moveable electrodes are located between two fixed electrodes, which are biased using two voltage supplies with equal magnitudes and opposite in direction. The device can be described by the following equivalent electrical circuit [14]:

$$V_{out} = -V_s + \frac{C_1}{C_1 + C_2}(2V_s) = \frac{C_1 - C_2}{C_1 + C_2}V_s \quad (12)$$

The capacitances C_1 and C_2 are not fixed due to the motion of the electrodes attached to the proof mass. When the moveable electrodes are at rest position, the two capacitances are equal and the output voltage is zero. However, under acceleration, the movable electrodes will displace and the gaps between fixed and movable electrodes will change by amount of δx. Thus, the output voltage as a function of displacement (δx), original gap (g_{ap}) and input voltage magnitude (V_s) can be written as:

$$V_{out} = \frac{\delta x}{g_{ap}}V_s \quad (13)$$

The relationship between displacement (δx) and acceleration (a) can be written as:

$$\delta x = \frac{ma}{k} = \frac{a}{\omega_0^2} \quad (14)$$

Hence, the relationship between the output voltage and the applied acceleration can be obtained as:

$$V_{out} = \frac{\delta x}{g_{ap}}V_s = \frac{a}{g_{ap}\omega_0^2}V_s \quad (15)$$

The V_{out} is then calculated using the design parameters for a given acceleration (10 to 50g) and the results are shown in Fig. 13. In addition, the output voltage is also estimated using the simulated displacement values obtained from COMSOL

software. From the Fig. 13, it can be seen that the analytically evaluated output voltages and simulated output voltages are very similar. The linear relationship, as shown in Fig. 13, is resulted from the linear dependence of output voltage with displacement.
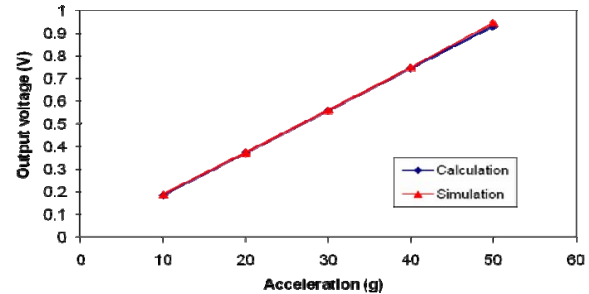

Fig. 13 Comparison of analytically calculated and simulated output voltages

B. Stability and sensitivity analysis of the structure

The purpose of the stability analysis is to check whether the movable electrodes will remain within the stable equilibrium range when the various accelerations are applied. If the net force approaches an unstable point, the electrodes would have the possibility to hit the fixed structures and/or brake away. At pull-in voltage, the displacement is equal to $g_{ap}/3$ and the magnitude of the pull-in voltage (V_{pi}) can be obtained as [14]:

$$V_{pi} = \sqrt{\frac{8kg_{ap}^3}{27\varepsilon A}} \quad (16)$$

Where k is the spring constant and A is the overlap area. Using Equation 16, it is found that the pull-in voltage of the proposed accelerometer is obtained as 33.1V. Thus, the input DC voltage of 7.58 V to achieve 150g during the self-test will not push the accelerometer into the unstable region.

The sensitivity of the accelerometer for a given acceleration can be estimated as [14]:

$$V_{out} = \frac{a}{g_{ap}\omega_0^2}V_s \quad (17)$$

Using the design parameters, the sensitivity of the accelerometer is found to be about 7.2 mV/g. This corresponded to an output voltage of 0.36 V at 50g acceleration. It can be seen from Equation (17) that the sensitivity is strongly dependent on the resonant frequency, which is further depended on the required bandwidth of operation.

VII. CONCLUSION

The characteristic of the impact acceleration due to a haversine wheel flat is investigated by a pitch plane vehicle model supported on the 3-layer modeled track. This study shows that wheel flat has significant influence on peak acceleration response in the vicinity of the wheel-rail contact zone due to the presence of the wheel flat.

In the design of the accelerometer, two main functions are performed. First, the sensing region is designed to measure the acceleration due to the changes in distance between the

electrodes. Second, a self-test region is designed within the accelerometer to facilitate self-tests of each individual accelerometer.

Finite element simulations are performed and their results are in very good agreement with the calculated results. The results from simple calculations vary 1% to 2% from the highly complex and time consuming simulations.

The current design resulted in a very high spring force, which is strong enough to prevent the movable electrodes from hitting the fixed electrodes under the largest foreseeable accelerations (150g). This is favorable for stability, as the current design will never reach the unstable region of operations.

REFERENCES

[1] Sun, Y.Q., and Dhanasekar, M., "A dynamic model for the vertical interaction of the rail track and wagon system" *International Journal of Solids and Structures* 39 (2002) 1337–1359.

[2] Ishida, M., and Ban, T., "Modelling of the wheel flats for track dynamics" *XXX Convegno Nazionale AIAS- Alghero (SS),* 12-15 September 2001.

[3] Jergeus, J., Odenmarck, C., Lunden, R., Sotkovszki, P., Karlsson, B., and Gullers, P., "Full-scale railway wheel flat experiments" *Proceedings of Institution of Mechanical Engineers* Volume 213 Part F, 1998,pp1-13.

[4] Zhai, W. M., Cai, C. B., Wang, Q. C., Lu, Z.W., and Wu., X. S., "Dynamic effects of Vehicles on Tracks in the case of raising train speed" *Proceedings of the Institution of Mechanical Engineers,* Part F, v 215, 2001, p125-135

[5] V. Belotti, F. Crenna, R. C. Michelini, and G. B. Rossi, "Wheel-flat diagnostic tool via wavelet transform" *Mechanical Systems and Signal Processing* 20 (2006) 1953–1966

[6] D. R. Anderson, "Detecting flat wheels with a Fiber-optic sensor" *Proceedings of Joint Rail Conference,* April 4-6, 2006, Atlanta, GA, USA

[7] Peter Hesser, Joe Noffsinger, and Tom Shanahan, "Precision Train Inspection Methods – North American Adoption of Global Technology" *General Electric Company*, 2005.

[8] http://www.freepatentsonline.com/4129276.html

[9] Dong, R.G., "Vertical dynamics of railway vehicle-track system*," Ph.D. Thesis,* Dept. of Mechanical and Industrial Engineering, Concordia University, Montreal, Canada, 1994.

[10] Zhai, W., and Cai, Z., "Dynamic interaction between a lumped mass vehicle and a discretely supported continuous rail track" *Computers and Structures* Vol. 63, No. 5, pp. 987-997, 1997.

[11] Yan, W., and Fischer, F.D., "Applicability of the Hertz contact theory to rail-wheel contact problems" *Archive of Applied Mechanics* 70 (2000) 255-268.

[12] Rajib Ul Alam Uzzal, "Role of Railway Vehicle-Track System and Design Parameters on Flat-Induced Impact Load" *M. A. Sc thesis*, Dept. of Mechanical & Industrial Engineering, Concordia University, Montreal, Quebec, Canada 2007.

[13] Lonsdale, C., Dedmon, S., and Pilch, J., "Effects of increased gross rail load on 36-inch diameter freight car wheels"availableat *www.standardsteel.com/rdpapers/2001*

[14] Stephen D. Senturia, "Microsystem Design", *Kluwer Academic Publishers,* 2001

[15] http://www.ee.ucla.edu/~wu/ee250b/Case%20study-apacitive%20Accelerometer.pdf